

See discussions, stats, and author profiles for this publication at: <https://www.researchgate.net/publication/263887682>

Thermal conductance imaging of graphene contacts

ARTICLE · JANUARY 2014

DOI: <http://dx.doi.org/10.1063/1.4889928>

CITATIONS

2

READS

53

9 AUTHORS, INCLUDING:



[Carlo Maragliano](#)

Masdar Institute of Science and Technology

26 PUBLICATIONS **86** CITATIONS

[SEE PROFILE](#)



[Marco Stefancich](#)

Masdar Institute of Science and Technology

112 PUBLICATIONS **731** CITATIONS

[SEE PROFILE](#)



[Matteo Chiesa](#)

Masdar Institute of Science and Technology

159 PUBLICATIONS **1,602** CITATIONS

[SEE PROFILE](#)



[Anna K Swan](#)

Boston University

156 PUBLICATIONS **3,172** CITATIONS

[SEE PROFILE](#)



Thermal conductance imaging of graphene contacts

Jia Yang, Elbara Ziade, Carlo Maragliano, Robert Crowder, Xuanye Wang, Marco Stefancich, Matteo Chiesa, Anna K. Swan, and Aaron J. Schmidt

Citation: *Journal of Applied Physics* **116**, 023515 (2014); doi: 10.1063/1.4889928

View online: <http://dx.doi.org/10.1063/1.4889928>

View Table of Contents: <http://scitation.aip.org/content/aip/journal/jap/116/2?ver=pdfcov>

Published by the [AIP Publishing](#)

Articles you may be interested in

[Thermal conductivity of hybrid graphene/silicon heterostructures](#)

J. Appl. Phys. **114**, 153518 (2013); 10.1063/1.4826492

[Anisotropic thermal conductivity of semiconducting graphene monoxide](#)

Appl. Phys. Lett. **102**, 223101 (2013); 10.1063/1.4808448

[How does folding modulate thermal conductivity of graphene?](#)

Appl. Phys. Lett. **100**, 093107 (2012); 10.1063/1.3690871

[Minimum thermal conductance in graphene and boron nitride superlattice](#)

Appl. Phys. Lett. **99**, 043109 (2011); 10.1063/1.3619832

[Lattice thermal conductivity of graphene flakes: Comparison with bulk graphite](#)

Appl. Phys. Lett. **94**, 203103 (2009); 10.1063/1.3136860

The logo for the Journal of Applied Physics, featuring the letters 'AIP' in a large, white, sans-serif font on the left, followed by a vertical line and the words 'Journal of Applied Physics' in a smaller, white, sans-serif font on the right. The background is a dark orange with a subtle, abstract pattern of light-colored, curved lines.
A small, square, head-and-shoulders portrait of a man with short, light-colored hair, wearing a light blue shirt. He is looking directly at the camera with a neutral expression.

Journal of Applied Physics is pleased to announce **André Anders** as its new Editor-in-Chief



Thermal conductance imaging of graphene contacts

Jia Yang,¹ Elbara Ziade,¹ Carlo Maragliano,² Robert Crowder,¹ Xuanye Wang,³ Marco Stefancich,² Matteo Chiesa,² Anna K. Swan,³ and Aaron J. Schmidt¹

¹Department of Mechanical Engineering, Boston University, Boston, Massachusetts 02215, USA

²Institute Center for Energy, Masdar Institute of Science and Technology, Abu Dhabi, United Arab Emirates

³Department of Electrical and Computer Engineering, Boston University, Boston, Massachusetts 02215, USA

(Received 3 June 2014; accepted 29 June 2014; published online 11 July 2014)

Suspended graphene has the highest measured thermal conductivity of any material at room temperature. However, when graphene is supported by a substrate or encased between two materials, basal-plane heat transfer is suppressed by phonon interactions at the interfaces. We have used frequency domain thermoreflectance to create thermal conductance maps of graphene contacts, obtaining simultaneous measurements of the basal-plane thermal conductivity and cross-plane thermal boundary conductance for 1–7 graphitic layers encased between titanium and silicon dioxide. We find that the basal-plane thermal conductivity is similar to that of graphene supported on silicon dioxide. Our results have implications for heat transfer in two-dimensional material systems, and are relevant for applications such as graphene transistors and other nanoelectronic devices. © 2014 AIP Publishing LLC. [<http://dx.doi.org/10.1063/1.4889928>]

I. INTRODUCTION

Two-dimensional (2D) materials have motivated extensive study because of their unique electronic and thermal properties.¹ Graphene,² the 2D form of graphite, has the highest measured thermal conductivity of any material at room temperature—using a Raman thermometry technique, Balandin and co-workers measured a basal-plane (in-plane) thermal conductivity, κ , for one suspended atomic layer of graphene in the range of 2000–5000 W m⁻¹ K⁻¹ depending on the size of the flake.³ The high thermal conductivity, which arises from extremely strong sp^2 bonding in the basal plane and unusually large phonon mean free path (MFP) of the long-wavelength phonons,^{4,5} makes graphene attractive for nanoelectronic device applications such as transistors, interconnects, and heat spreaders.^{6,7} However, in these applications, graphene is in contact with other materials, and previous measurements have reported that the heat flow in graphene is suppressed not only through the graphene channel,^{8,9} but also across metal contacts¹⁰ due to phonon interactions at the interfaces.

Based on a thermal bridge method, Seol *et al.* and Sadeghi *et al.* reported 600 W m⁻¹ K⁻¹ for κ of single-layer graphene supported by SiO₂ at room temperature and the value increased with additional layers, up to 34 layers, approaching but not reaching the value of the graphite exfoliation source.^{8,11} Measurement of κ for encased graphene is more challenging due to the lack of direct access. Using metallic heaters, Jang *et al.* showed that for graphene encased by SiO₂, the top oxide layer further reduced κ to below 160 W m⁻¹ K⁻¹.⁹ In the cross-plane direction, the thermal boundary conductance (TBC) across graphene interfaces was measured to be 20–30 MW m⁻² K⁻¹ by Koh *et al.* based on time-domain thermoreflectance (TDTR),¹⁰ lower than that of metal/dielectric interfaces. However, despite the importance of graphene-metal contacts in device design,¹² the thermal

conductivity of metal-coated graphene has not been measured.

In this paper, we describe frequency domain thermoreflectance (FDTR) imaging¹³ of encased graphene, using thermal waves from 100 kHz to 50 MHz to image sub-surface graphitic multilayers and create micron-scale maps of the in-plane thermal conductance and TBC of two mechanically exfoliated graphene flakes encased between Ti and SiO₂. The obtained values indicate that depositing Ti has no significant impact on the thermal conductivity of graphene exfoliated on SiO₂.

II. EXPERIMENTAL

Figure 1 shows a schematic of our sample configuration and experimental setup. Graphene flakes were encased between a metal layer and a thermally oxidized p-type silicon wafer. A periodically modulated continuous-wave laser (the pump beam) is focused to a Gaussian spot with a 1.6 μm 1/e² diameter while a second, unmodulated laser beam was used to measure the surface temperature through a proportional change in reflectivity. We vary the pump beam modulation frequency and measure the phase lag of the probe signal using a lock-in amplifier. Unknown thermal properties of the sample are extracted by minimizing the error between the phase data and an analytical solution to the heat diffusion equation. Our multilayer diffusion model, described in Ref. 14, calculates the frequency response of the surface temperature to the pump beam, and includes cross-plane and radial transport as well as the TBC between each layer. Because our model is based on Fourier's law of heat conduction, the property values we obtain are effective diffusion transport properties. The room temperature phonon MFP has been estimated with the 2D kinetic theory to be 775 nm for suspended single-layer graphene,¹⁵ and 10–50 nm for graphene encased between SiO₂.⁹ Since this is significantly smaller than our pump laser spot diameter, a diffusive model is suitable.

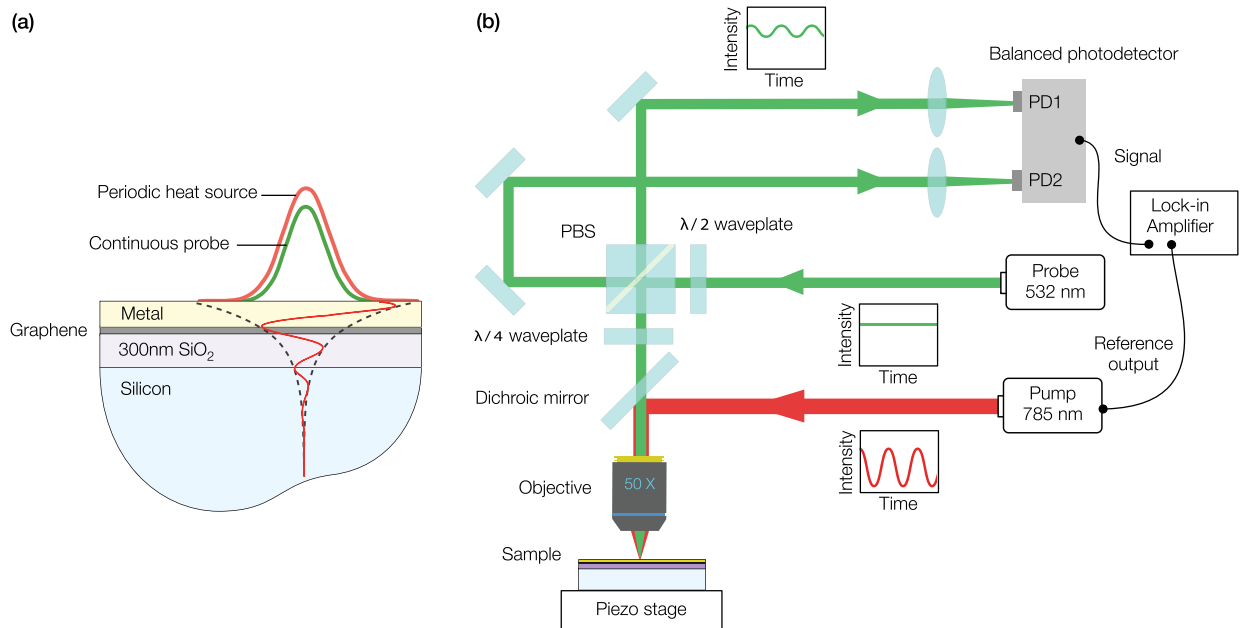


FIG. 1. Sample configuration and experimental setup. (a) Sample configuration of encased graphene flakes during FDTR imaging. The sample consists of four layers: a 50–100 nm metal coating, an exfoliated graphene flake, 300 nm of thermal SiO₂, and a p-type silicon substrate. (b) Schematic of our FDTR microscope. A digitally modulated pump laser heats the sample while a probe beam monitors the surface reflectivity. A balanced photodetector is used to improve the signal to noise ratio. A piezo stage is used to raster scan the sample for imaging.

A. Sample preparation

We prepared two graphene samples by mechanical exfoliation of bulk graphite onto thermally oxidized p-type silicon substrates. The target thickness of the SiO₂ layer was chosen to be ~300 nm to maximize the contrast of graphene flakes under an optical microscope. After mechanical exfoliation, the two samples were annealed at 400 °C for 2 hours in forming gas to remove adhesive residue from the tape.¹⁶ Optical images of the samples are shown in Figs. 2(a) and 2(b). The number of graphene layers within the flakes, labeled on each flake image, was determined by optical contrast and atomic force microscopy (AFM). For flake

1, the substrate was fresh. For flake 2, the substrate was used for mechanical exfoliation multiple times and between each exfoliation we cleaned the substrate with oxygen plasma ashing and piranha solution (sulfuric acid and hydrogen peroxide, 3:1). AFM images of the flake substrates showed similar surface roughness, but flake 2 had a significant amount of debris with a root mean square (RMS) roughness of ~1 nm, shown in the AFM image of Fig. 2(b). After AFM characterization, we deposited a thin layer of metal with electron-beam evaporation. Flake 1 was coated with a 10 nm Ti adhesion layer followed by 46 nm of Au without breaking vacuum, while flake 2 was coated with 65 nm of Ti.

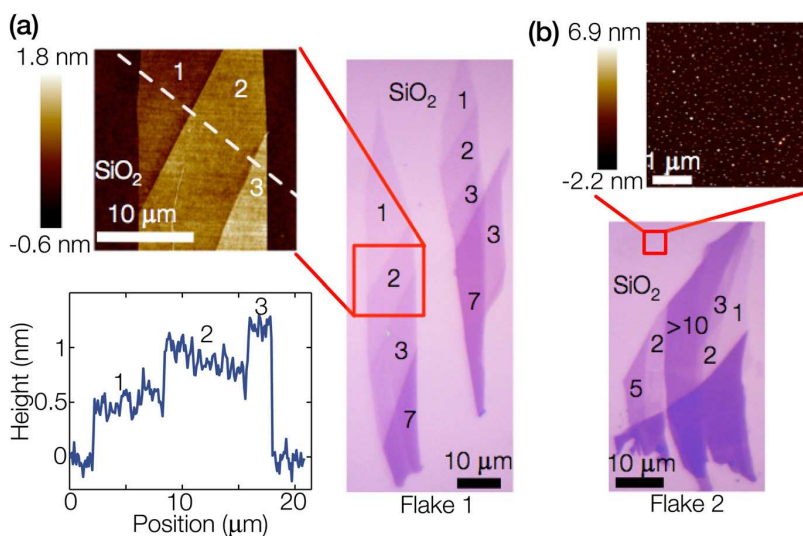


FIG. 2. Graphene samples. (a) Optical image of flake 1 together with an AFM image of the region indicated with a red box. The height profile along the dashed line shows one, two, and three layers of graphene sheets. (b) Optical image of flake 2 together with an AFM image of the oxide region showing contaminant particles. The number of graphene layers is labeled on the flakes.

III. RESULTS AND DISCUSSION

We acquired thermal phase images by scanning the sample stage in two dimensions while recording phase data from the lock-in amplifier at six frequencies simultaneously. Maps of the in-plane thermal conductance, G_{\parallel} , and the TBC were created by performing a two-parameter fit of our diffusion model to the six phase data points at each pixel, after the properties of the other layers in the stack had been determined with additional measurements on reference samples. Here, we use flake 1 as an example to show the measurement procedure.

A. Parameter fitting

The configuration of flake 1, shown in Fig. 3(a), includes four layers: Au/Ti, graphene, SiO_2 , and p-type silicon. We treat graphene as a layer with zero heat capacity, because the thermal time constant of the graphene layer is much shorter than the heating period in our measurements.⁷ We also neglect the interface between Au and Ti and treat them as a single layer, since the TBC for metal-metal interfaces has been measured to be an order of magnitude higher than that for semiconductor and dielectric interfaces.¹⁷ Figure 3(b)

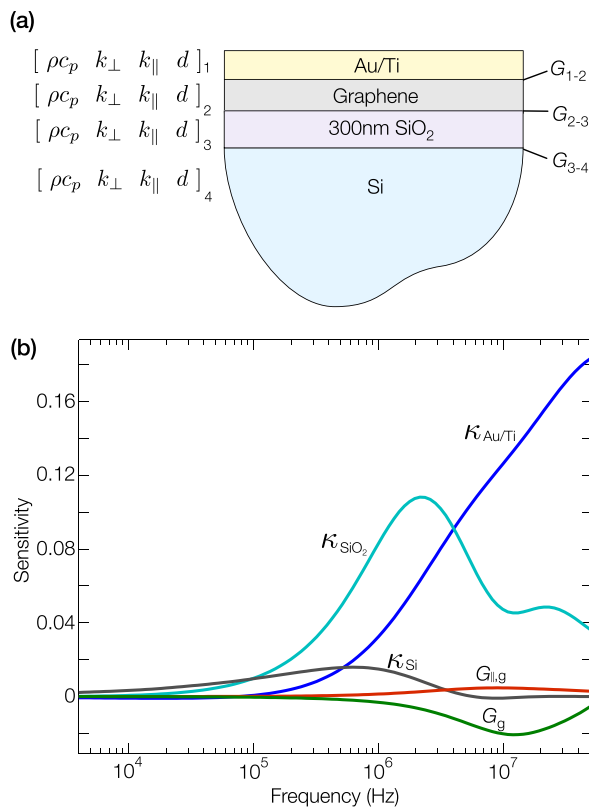


FIG. 3. Sample configuration and sensitivity. (a) Flake 1 consists of four layers: Au/Ti, graphene, 300 nm SiO_2 , and p-type Si substrate. Each layer has five physical parameters: the volumetric heat capacity, ρc_p , the cross-plane and in-plane thermal conductivities, κ_{\perp} and κ_{\parallel} , the layer thickness, d , and the TBC to the next layer, G . (b) Calculated sensitivity to the thermal conductivity of Au/Ti, $\kappa_{\text{Au/Ti}}$, the thermal conductivity of SiO_2 , κ_{SiO_2} , the thermal conductivity of silicon, κ_{Si} , in-plane thermal conductance, and the TBC of graphene layer, $G_{\parallel,g}$ and G_g .

shows the calculated sensitivity of the phase signal to G_{\parallel} and the TBC of graphene layer and the next three most dominant parameters in the thermal model. The sensitivity to a property x was calculated from $\partial\phi/\partial\ln x$, where ϕ is calculated with the thermal model using pump and probe spot radii of $0.8 \mu\text{m}$ and $0.7 \mu\text{m}$, respectively.

To determine the thermal properties and thicknesses of all layers other than graphene, we co-deposited several reference samples of fused silica (thermal diffusivity $= 8.46 \times 10^{-7} \text{m}^2/\text{s}$ at 300 K, Ref. 18), and pieces of the p-type silicon wafer with thermal oxide that was used for our graphene samples. The total thickness of Au/Ti on flake 1 is 62 nm, while the thickness of Ti on flake 3 is 65 nm, measured by AFM on reference glass slides. The oxidized p-type silicon wafer was purchased from University Wafer, Inc. The thickness of SiO_2 was measured to be 296 nm by ellipsometry. The κ of the p-type silicon was measured by FDTR. We first etched away the oxide by immersing one piece of the substrate in buffered oxide etchant (BOE, 6:1) for 3 min. The substrate was left in air overnight and then coated with 74 nm of Au by electron-beam evaporation. The thermal conductivity was then measured to be $80 \text{W m}^{-1} \text{K}^{-1}$.

Because the metal thermal conductivity is the most critical parameter, we took several steps to determine it as accurately as possible. We first measured the in-plane thermal conductivity, κ , and electrical conductivity, σ , of the Au/Ti film on the reference samples by FDTR with three spot sizes

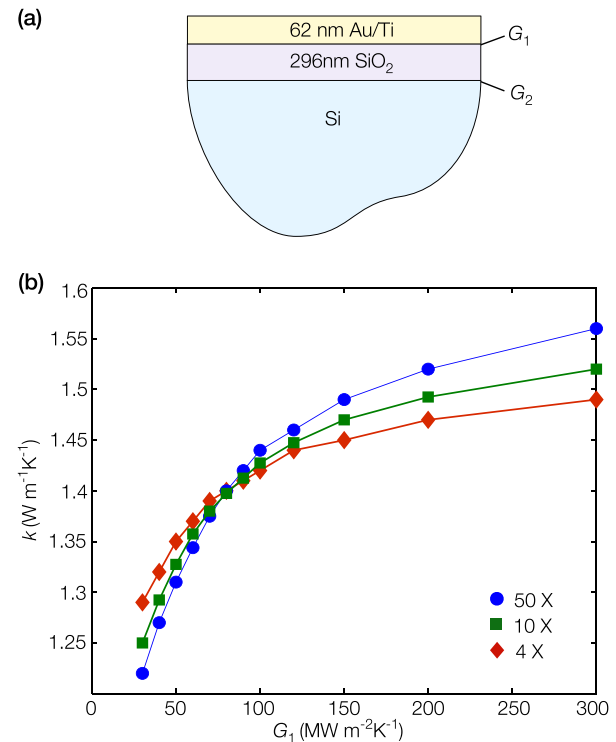


FIG. 4. Thermal conductivity measurement of SiO_2 . (a) Sample configuration of the reference sample. Included are also the TBC between Au/Ti and SiO_2 , G_1 , and the TBC between SiO_2 and silicon, G_2 . (b) κ of SiO_2 vs. G_1 measured with 50 \times , 10 \times , and 4 \times objectives.

TABLE I. Fitting parameters for graphene samples.

Material	ρc_p ($10^6 \text{ J m}^{-3} \text{ K}^{-1}$)	κ ($\text{W m}^{-1} \text{ K}^{-1}$)	d (nm)
Au/Ti	2.49 (Ref. 18)	140 ± 4	62
Ti	2.38 (Ref. 18)	5.8 ± 0.4	65
SiO ₂	1.63 (Ref. 18)	1.4	296
P-type silicon	1.65 (Ref. 18)	80	5×10^5

and a four-point probe, respectively. An effective Lorenz number was calculated using the Wiedemann-Franz law: $L = \kappa/\sigma T = 2.43 \times 10^{-8} \Omega \text{ W K}^{-2}$, where T is the absolute temperature.¹⁹ This Lorenz number was then used to convert four-point probe electrical conductivity measurements from the oxide regions of flake 1 to a thermal conductivity of $140 \pm 4 \text{ W m}^{-1} \text{ K}^{-1}$, based on 23 measured values of σ .

The thermal conductivity of SiO₂ was measured by FDTR on a p-type silicon reference sample using the determined κ values of Au/Ti and p-type silicon. Figure 4(a) shows the reference sample configuration. The κ of SiO₂ and the top and bottom TBCs, G_1 and G_2 , contribute to the thermal resistance of the SiO₂ layer. Based on the reported thermal interface resistance values of thermally grown SiO₂ on silicon,²⁰ we took G_2 to be $120 \text{ MW m}^{-2} \text{ K}^{-1}$. To separate κ of SiO₂ and G_1 , we performed FDTR on the sample with three spot sizes using a $50\times$ objective (NA = 0.55), $10\times$ objective (NA = 0.25), and $4\times$ objective (NA = 0.1). The pump and probe spot radii were $0.8 \mu\text{m}$ and $0.7 \mu\text{m}$, respectively, for the $50\times$ objective, and

$2.8 \mu\text{m}$ and $1.6 \mu\text{m}$, respectively, for the $10\times$ objective, while those for the $4\times$ objective are $6.8 \mu\text{m}$ and $3.6 \mu\text{m}$, respectively.

By fitting the data from all three measurements simultaneously, there is sufficient sensitivity to determine both κ of SiO₂ and G_1 . Alternatively, we can fit the data set at each spot size with a series of $\kappa - G_1$ pairs obtained with single-parameter fitting. For any two spot sizes, only a single $\kappa - G_1$ pair will match both sets of data. This is shown in Fig. 4(b), where G_1 was varied from $30 \text{ MW m}^{-2} \text{ K}^{-1}$ to $300 \text{ MW m}^{-2} \text{ K}^{-1}$ for data at three spot sizes and the corresponding κ values of SiO₂ were obtained by single-parameter fitting. The intersection gives $\kappa = 1.4 \text{ W m}^{-1} \text{ K}^{-1}$ for SiO₂ and $G_1 = 80 \text{ MW m}^{-2} \text{ K}^{-1}$. Our κ value agrees to better than 3% with the reported value in Ref. 9 and G_1 is consistent with the measured value in Ref. 10.

The laser spot radii are also sensitive parameters in our thermal model. We fit the effective spot radii to match phase data from the fully characterized reference samples. By using the piezo z-stage, we could repeatedly focus the pump and probe spot radii to within 10 nm by maximizing the thermal signal. Values were similar to 2D knife-edge measurements but had ~ 5 times less variation. The fitted spot sizes, together with κ of the metal coating and all the other measured parameters, were then used to fit the graphene thermal conductance images. All the parameters for the graphene samples are summarized in Table I. The thermal conductivity of the 65 nm Ti on flake 2 was measured by FDTR directly on flake 2 in the regions without

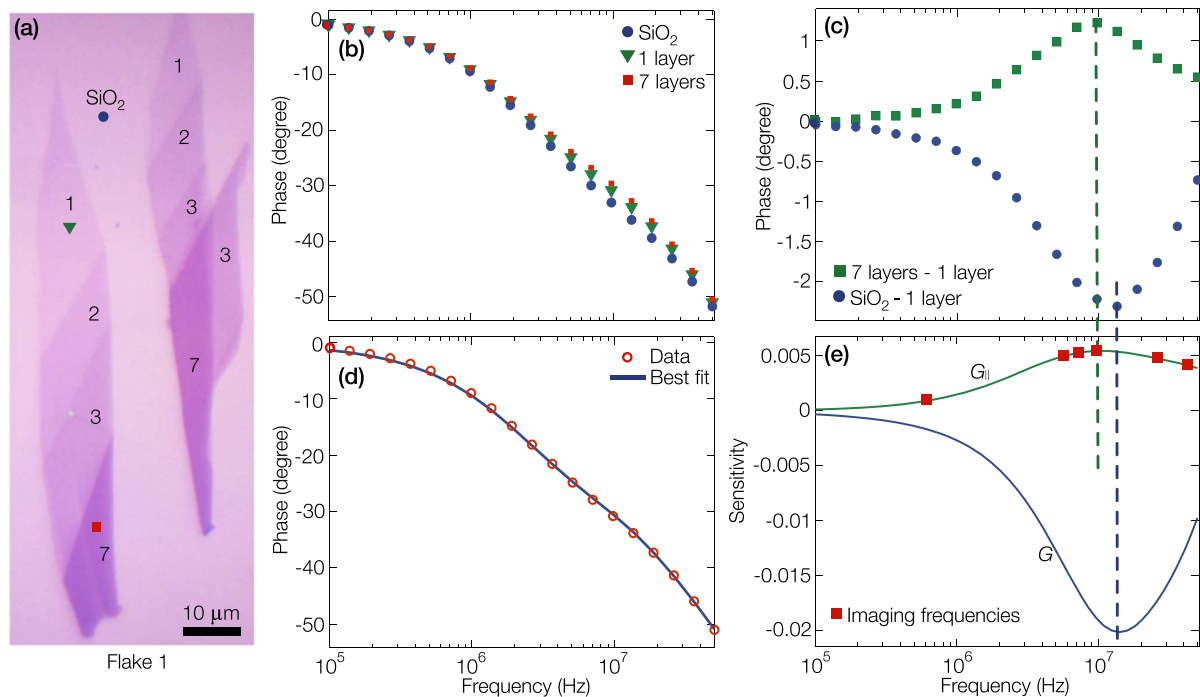


FIG. 5. Sensitivity analysis. (a) Optical image flake 1. (b) FDTR data acquired after metal coating from the three regions of flake 1 indicated in (a): SiO₂ substrate, single-layer graphene and seven-layer graphene. (c) Difference between phase data from single-layer and seven-layer graphene (green squares), and between single-layer graphene and the SiO₂ substrate (blue circles). (d) Phase data of single-layer graphene from (b) and typical best fit of our thermal model. (e) Calculated phase sensitivity to graphene in-plane thermal conductance, G_{\parallel} , and to the TBC, G , of the Au/Ti/graphene/SiO₂ interface. The six frequency points used for imaging are shown as red squares.

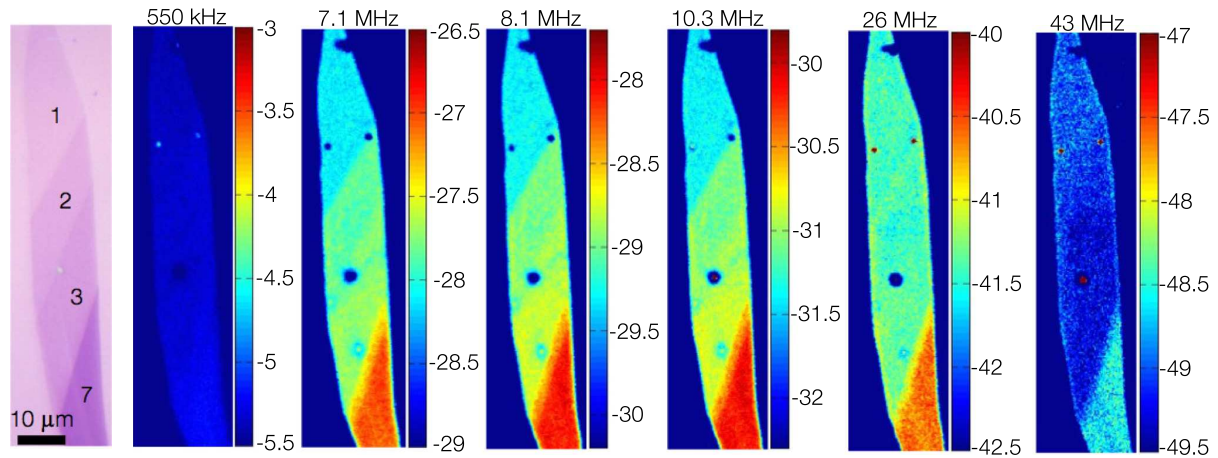


FIG. 6. Phase images of flake 1 acquired simultaneously at six frequencies: 550 kHz, 7.1 MHz, 8.1 MHz, 10.3 MHz, 26 MHz, and 43 MHz. The image contrast between the layers follows the sensitivity to G_{\parallel} shown in Fig. 5(e).

graphene, using the previously measured values of SiO_2 and silicon.

B. Imaging graphene

In order to analyze the sensitivity of our measurement to the graphene layer, we performed single-point FDTR measurements using 20 frequencies at several locations on the flakes. The microscope objective was $50\times$ with pump and probe $1/e^2$ spot radii of $0.8\ \mu\text{m}$ and $0.7\ \mu\text{m}$, respectively. In Fig. 5(b), we plot the phase data acquired from three regions on flake 1: the SiO_2 substrate without graphene, single-layer graphene, and seven-layer graphene. To highlight the differences between the three sets of data, we plot the difference between substrate and single-layer graphene data, and the difference between single-layer and seven-layer graphene data, in Fig. 5(c). The phase difference at each frequency between different regions can be represented as $\sum_{i=1}^N \frac{\partial \phi(\omega)}{\partial x_i} \Delta x_i$, where Δx_i is the change in property x_i and N is the total number of parameters in the thermal model. When there is a dominant change in one thermal property within the sample, the shape of difference data will match the phase sensitivity to that property. In Fig. 5(e), we plot the calculated phase sensitivity to the in-plane graphene conductance and to the cross-plane graphene conductance. The close agreement between the shapes of the curves in Figs. 5(c) and 5(e) shows that the change in signal from single-layer graphene to the substrate is primarily from the change in cross-plane conductance, while the change from single-layer to seven-layer graphene is mainly due to the in-plane conductance, consistent with previous cross-plane measurements that showed a minimal change due to additional graphene layers.¹⁰

Figure 5(d) shows a typical best fit of our model to a region of single-layer graphene, where we have used nonlinear least squares minimization to simultaneously determine the thermal conductivity to be $617\ \text{W m}^{-1}\ \text{K}^{-1}$ for single-layer graphene (assuming a thickness of $0.35\ \text{nm}$ for a monolayer of graphene²¹) and the TBC to be $22\ \text{MW m}^{-2}\ \text{K}^{-1}$ for the Au/Ti/single-layer graphene/ SiO_2 interface.

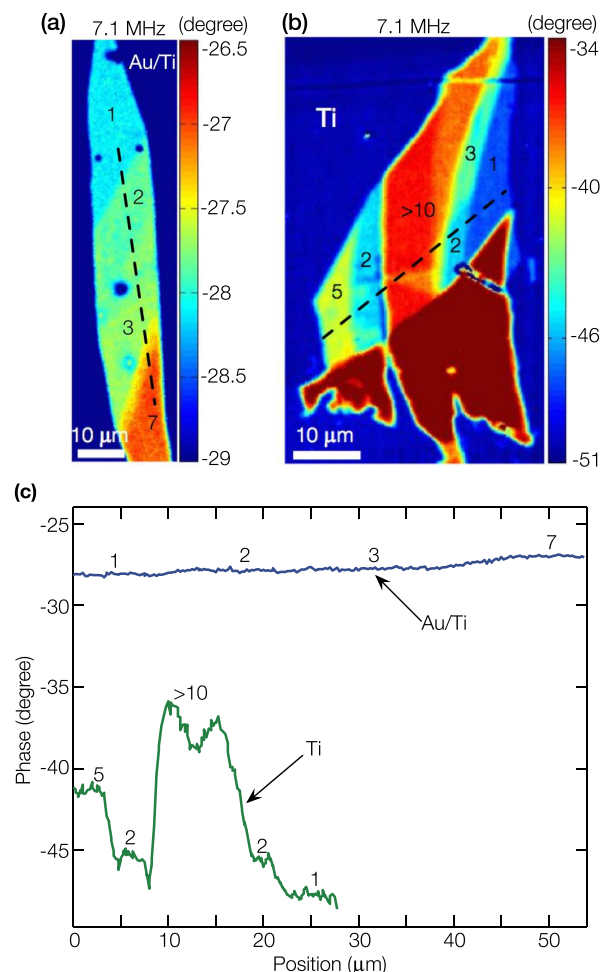


FIG. 7. Phase image comparison between flake 1 and flake 2. (a) Phase image of flake 1 at 7.1 MHz. (b) Phase image of flake 2 at 7.1 MHz. (c) Phase profiles along the two dashed lines in (a) and (b), showing enhanced sensitivity to radial transport in graphene due to the low thermal conductivity of the Ti film.

To generate thermal property maps, we simultaneously acquired phase images at six frequencies for each graphene sample, selected based on the sensitivity to G_{\parallel} as shown in Fig. 5(e). In Fig. 6, we show the six phase images taken for one portion of flake 1. The trend of image contrast between graphene layers agrees well with the calculated sensitivity to G_{\parallel} : contrast is low at the lowest frequency, arrives at a peak at 10.3 MHz, then decreases at the highest frequency.

Although the different layers are quite clear in Fig. 6, the difference between the highest and lowest phase in each image is only 2.5° . To explain the small phase difference between layers, we temporarily neglect heat transfer in the substrate and approximate in-plane heat transfer in the metal film and graphene with a one-dimensional thermal resistance network composed of two parallel elements $R = (\kappa d)^{-1}$, where κ is the in-plane thermal conductivity and d is the thickness of the layer. Putting in our measured numbers for the Au/Ti film ($d = 62$ nm, $\kappa = 140$ W m $^{-1}$ K $^{-1}$) and the reported values for single-layer graphene on SiO $_2$ ($d = 0.35$ nm, $\kappa = 600$ W m $^{-1}$ K $^{-1}$, Ref. 8), we see that only 2.4% of the heat is conducted through the graphene, while the remainder is conducted through the Au/Ti film. To enhance the heat flow in the graphene layer, and consequently decrease our experimental uncertainty, flake 2 was coated with 65 nm

of Ti. The Ti film had a thermal conductivity of 5.8 W m $^{-1}$ K $^{-1}$, as shown in Table I. Repeating the calculation with the Ti values, we find the percentage of heat conducted in the graphene layer is increased to 36%. Enhanced sensitivity to radial transport is confirmed by comparing phase images from flake 1 and flake 2 at the same frequency in Fig. 7. Although the signal-to-noise ratio is lower for flake 2 (due to the lower coefficient of thermoreflectance of Ti compared to Au at 532 nm), the increased sensitivity significantly reduced uncertainty in determining κ of encased single-layer graphene.

The thermal conductance maps for the two samples are shown in Fig. 8. The in-plane thermal conductance values for each layer were converted to thermal conductivities using $\kappa = G_{\parallel}/nt$, where n is the number of layers and $t = 0.35$ nm is the thickness of monolayer graphene.²¹ We used pixel statistics to calculate error bars, selecting regions with constant layer thickness and fitting the resulting histograms with normal distributions. This accounts for all sources of statistical noise in the measurement.

To account for the additional uncertainty introduced by the values of physical properties in our thermal model, we fit the property maps three times using the upper bound, average, and lower bound of the metal layer thermal conductivity, which was by far the largest factor affecting the fitted values.

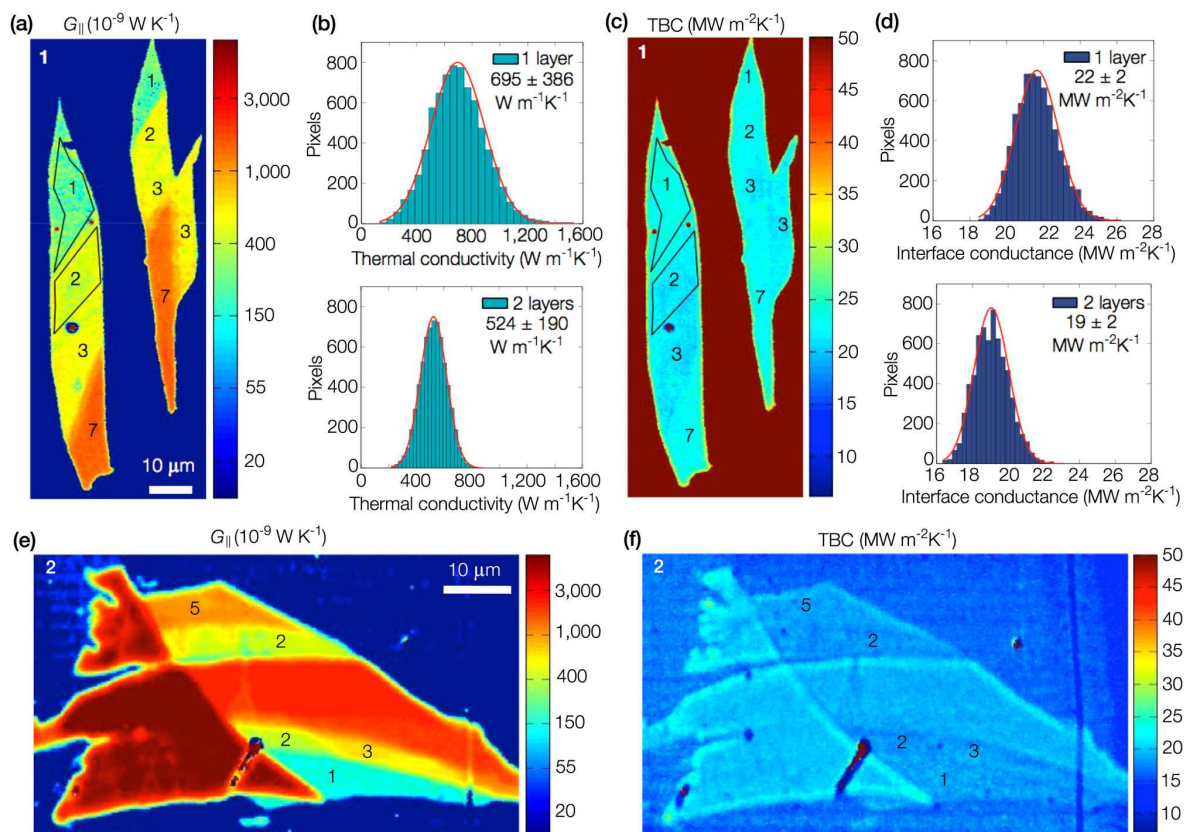


FIG. 8. Thermal conductance maps of the two samples. (a) G_{\parallel} map of flake 1. (b) Histograms of the thermal conductivity for single-layer graphene and bi-layer graphene analyzed from the polygons in (a). (c) TBC map of flake 1. (d) Histograms of TBC of single-layer graphene and bi-layer graphene, analyzed from the polygons in (c). (e) G_{\parallel} map of flake 2. (f) TBC map of flake 2. The upper limit of the color bars for (c) is set at 50 MW m $^{-2}$ K $^{-1}$ to highlight the graphene flake, although the measured value of TBC for Au/Ti/SiO $_2$ for this sample was closer to 100 MW m $^{-2}$ K $^{-1}$. The solid red lines in (b) and (d) are normal distribution fits.

In addition, we found that fitting effective spot sizes with the thermal model on the well calibrated silicon reference sample reduces the uncertainty in graphene values. We first fit three sets of effective pump and probe spot radii for our $50\times$ objective with our thermal model on the silicon reference sample, using $136\text{ W m}^{-1}\text{ K}^{-1}$, $140\text{ W m}^{-1}\text{ K}^{-1}$, and $144\text{ W m}^{-1}\text{ K}^{-1}$ as the thermal conductivity of the Au/Ti layer. Figure 9(a) shows the fitted in-plane thermal conductance maps corresponding to the three sets of κ and spot sizes. The pixel data from the selected regions, such as the single layer labeled by the dashed boxes in Fig. 9(a), were converted to thermal conductivity values by dividing with the thickness of monolayer graphene. The three thermal conductivity data histograms, shown in Fig. 9(b), are very close to each other, indicating that statistical noise dominates the uncertainty. The three histograms were then combined in Fig. 9(b) to get the total distribution. We define the average as the measured value and twice the standard deviation as the uncertainty. All the data analyses for flake 1 and flake 2 including the oxide regions without graphene were performed based on this procedure. The resulting values for the TBC and thermal conductivity of the two flakes are summarized in Fig. 10.

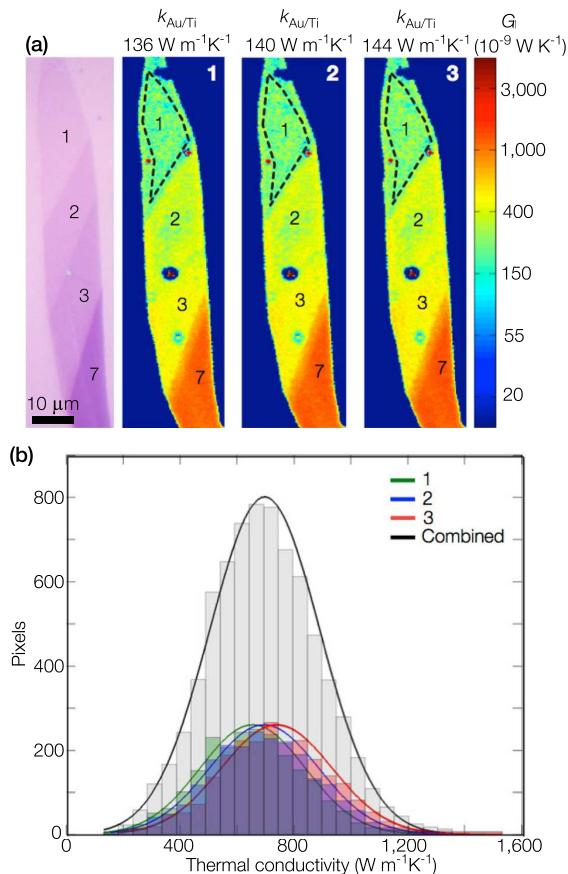


FIG. 9. Uncertainty analysis. (a) In-plane thermal conductance $G_{||}$ maps of flake 1 fitted with three κ values of Au/Ti. The images are labeled from left to right as 1, 2, and 3. (b) The thermal conductivity data histograms converted from the conductance pixel data in the labeled polygons of (a). The grey histogram is the total data distribution by combining all three histograms together. The colored lines are fits to the normal distribution.

C. Discussion

Considering first the TBC values in Fig. 10(a), for flake 1, the presence of graphene significantly reduces the TBC compared to that of the metal/SiO₂ interface of the surrounding substrate (zero layers). For flake 2, the zero-layer TBC is almost an order of magnitude lower than that for flake 1. This is likely due to the contaminating nanoparticles shown in Fig. 2(b), since a surface roughened by nanoparticles has been shown to reduce the TBC between a metal and a substrate.²³ In this case, the graphene improved cross-plane heat transfer. A possible explanation for the enhancement is that graphene conformed to the contours of the contaminated surface,^{24,25} increasing the thermal coupling between Ti and SiO₂.

From TDTR measurements from 50 to 500 K, Koh *et al.* found that heat flow across the graphene interface is governed by the Kapitza thermal resistances of the metal/

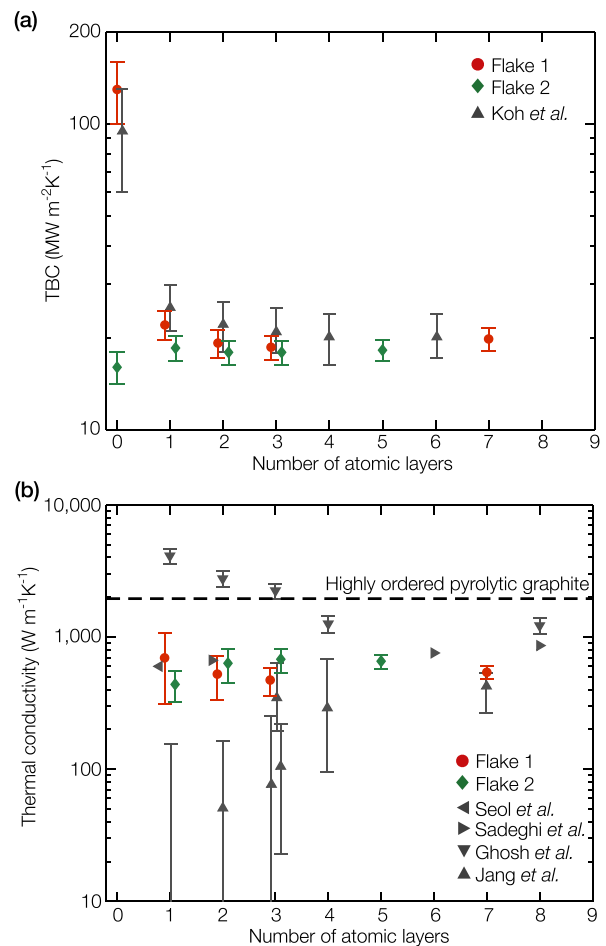


FIG. 10. Property values of single-layer graphene and few-layer graphene. (a) TBC for our samples and literature values for TBC of Au/Ti/graphene/SiO₂ (up triangles).¹⁰ (b) κ of the two samples as a function of the number of atomic layers. The layer coordinates have been offset slightly for clarity. For comparison, literature values are also shown for highly ordered pyrolytic graphite (dashed line),¹⁸ suspended single-layer and few-layer graphene (inverted triangles),²² single-layer graphene supported on SiO₂ (left triangles),⁸ few-layer graphene supported on SiO₂ (right triangles),¹¹ and single- and few-layer graphene encased between two SiO₂ layers (up triangles).⁹ Error bars indicate 95% confidence based on three pixel histograms.

graphene and graphene/SiO₂ interfaces acting in series: $G_{\text{total}}^{-1} = G_{\text{metal/graphene}}^{-1} + G_{\text{graphene/SiO}_2}^{-1}$.¹⁰ By approximating $G_{\text{metal/graphene}}$ with $G_{\text{metal/graphite}} = 46 \text{ MW m}^{-2} \text{ K}^{-1}$, which we measured with FDTR for Ti deposited on our natural graphite source, we estimate G of the single-layer graphene/SiO₂ interface to be $42 \text{ MW m}^{-2} \text{ K}^{-1}$ and $31 \text{ MW m}^{-2} \text{ K}^{-1}$ for flake 1 and flake 2, respectively, comparable to values reported in Refs. 26 and 27. For the two samples, TBC of the single-layer graphene/SiO₂ interface is higher than that of few-layer graphene/SiO₂ interfaces, i.e., 30% higher for flake 1 and 7% higher for flake 3. Prasher has shown theoretically that the TBC of a van der Waals (vdW) contact depends positively on the adhesion energy of the interface,²⁸ implying that the adhesion energy between single-layer graphene and SiO₂ is larger than that between few-layer graphene and SiO₂, consistent with the measurement in Ref. 25 that adhesion energy between multilayer graphene and SiO₂ drops from 0.45 J m^{-2} to 0.31 J m^{-2} when the layer number increases from one to two or more.

Turning to the in-plane results in Fig. 10(b), our values are similar to those reported for single- and few-layer graphene supported on SiO₂ (Refs. 8 and 11) and higher than values reported for single- and few-layer graphene encased by two layers of SiO₂,⁹ suggesting that depositing Ti on graphene that had already conformed to the SiO₂ substrate^{24,25} has no significant impact on the basal-plane thermal conductivity.

We estimated the phonon MFPs in single-layer graphene and few-layer graphene for our graphene samples using the 2D kinetic theory: $\kappa = (1/2)Cv\Lambda$, where κ is the thermal conductivity, C is the volumetric heat capacity, v is the averaged phonon velocity, Λ is the phonon MFP, and the factor 1/2 is due to the 2D nature of graphene.¹⁵ This simplified expression is based on the gray approximation that all phonons have the same group velocity and lifetime. Because the transverse acoustic (TA) and longitudinal acoustic (LA) phonon modes in graphene have linear dispersions near the zone center²⁹ and our measurement temperature is well below graphite's Debye temperature ($\sim 2000 \text{ K}$ in-plane³⁰), this simple kinetic theory is suitable for estimating the phonon MFPs in graphene. We used $C = 1.57 \times 10^6 \text{ J m}^{-3} \text{ K}^{-1}$ at 300 K from the volumetric heat capacity of graphite.¹⁸ v is an average of LA and TA phonon velocities in graphene using $\frac{1}{v^2} = \frac{1}{2} \left(\frac{1}{v_{\text{LA}}^2} + \frac{1}{v_{\text{TA}}^2} \right)$,³¹ where $v_{\text{LA}} = 21.3 \text{ km s}^{-1}$ and $v_{\text{TA}} = 13.6 \text{ km s}^{-1}$ were taken from Ref. 29. Using these literature values and our measured κ values, we derived the room temperature Λ and summarized the results in Table II.

TABLE II. Estimated room temperature phonon MFPs in our graphene samples.

Sample	Phonon MFPs	
	Single-layer (nm)	Few-layer (nm)
Flake 1	55	42
Flake 2	34	51

IV. CONCLUSIONS

In conclusion, we have described a method for imaging sub-surface graphene in multilayer systems, and we have presented quantitative maps of both in-plane and cross-plane thermal conductance for single-layer graphene and few-layer graphene encased between a metal and SiO₂, obtaining definite values for κ of encased single-layer graphene. We found that graphene decreased the TBC between Ti and SiO₂ for clean interfaces, but enhanced the conductance for a contaminated interface. Comparison with reported κ for graphene supported on SiO₂ suggests a minimal impact from the deposited Ti on the thermal conductivity of graphene encased by Ti and SiO₂.

ACKNOWLEDGMENTS

Fabrication and experiments were carried out in the Boston University Photonics Center. We would like to thank M. Luckyanova and Dr. J. Cuffe for the use of the 50 \times objective. This work has been supported by the Trustees of Boston University.

- ¹S. Z. Butler, S. M. Hollen, L. Cao, Y. Cui, J. A. Gupta, H. R. Gutiérrez, T. F. Heinz, S. S. Hong, J. Huang, A. F. Ismach, E. Johnston-Halperin, M. Kuno, V. V. Plashnitsa, R. D. Robinson, R. S. Ruoff, S. Salahuddin, J. Shan, L. Shi, M. G. Spencer, M. Terrones, W. Windl, and J. E. Goldberger, "Progress, challenges, and opportunities in two-dimensional materials beyond graphene," *ACS Nano* **7**, 2898 (2013).
- ²K. S. Novoselov, A. K. Geim, S. V. Morozov, D. Jiang, Y. Zhang, S. V. Dubonos, I. V. Grigorieva, and A. A. Firsov, "Electric field effect in atomically thin carbon films," *Science* **306**, 666 (2004).
- ³A. A. Balandin, "Thermal properties of graphene and nanostructured carbon materials," *Nature Mater.* **10**, 569 (2011).
- ⁴D. L. Nika, S. Ghosh, E. P. Pokatilov, and A. A. Balandin, "Lattice thermal conductivity of graphene flakes: Comparison with bulk graphite," *Appl. Phys. Lett.* **94**, 203103 (2009).
- ⁵D. L. Nika, E. P. Pokatilov, and A. A. Balandin, "Theoretical description of thermal transport in graphene: The issues of phonon cut-off frequencies and polarization branches," *Phys. Status Solidi B* **248**, 2609 (2011).
- ⁶M. H. Bae, S. Islam, V. E. Dorgan, and E. Pop, "Scaling of high-field transport and localized heating in graphene transistors," *ACS Nano* **5**, 7936 (2011).
- ⁷E. Pop, V. Varshney, and A. K. Roy, "Thermal properties of graphene: Fundamentals and applications," *MRS Bull.* **37**, 1273 (2012).
- ⁸J. H. Seol, A. L. Moore, L. Shi, I. Jo, and Z. Yao, "Two-dimensional phonon transport in supported graphene," *Science* **328**, 213–216 (2010).
- ⁹W. Jang, Z. Chen, W. Bao, C. N. Lau, and C. Dames, "Thickness-dependent thermal conductivity of encased graphene and ultrathin graphite," *Nano Lett.* **2010**, 3909.
- ¹⁰Y. K. Koh, M. H. Bae, D. G. Cahill, and E. Pop, "Heat conduction across monolayer and few-layer graphenes," *Nano Lett.* **10**, 4363 (2010).
- ¹¹M. M. Sadeghi, I. Jo, and L. Shi, "Phonon-interface scattering in multilayer graphene on an amorphous support," *Proc. Natl. Acad. Sci. U.S.A.* **110**, 16321 (2013).
- ¹²K. L. Grosse, M. H. Bae, F. Lian, E. Pop, and W. P. King, "Nanoscale Joule heating, Peltier cooling and current crowding at graphene-metal contacts," *Nat. Nanotechnol.* **6**, 287 (2011).
- ¹³J. Yang, C. Maraglino, and A. J. Schmidt, "Thermal property microscopy with frequency domain thermoreflectance," *Rev. Sci. Instrum.* **84**, 104904 (2013).
- ¹⁴A. J. Schmidt, R. Cheaito, and M. Chiesa, "A frequency-domain thermoreflectance method for the characterization of thermal properties," *Rev. Sci. Instrum.* **80**, 094901 (2009).
- ¹⁵S. Ghosh, I. Calizo, D. Teweldebrhan, E. P. Pokatilov, D. L. Nika, A. A. Balandin, W. Bao, F. Miao, and C. N. Lau, "Extremely high thermal conductivity of graphene: Prospects for thermal management applications in nanoelectronic circuits," *Appl. Phys. Lett.* **92**, 151911 (2008).

- ¹⁶X. Wang, J. Li, Q. Zhong, Y. Zhong, and M. Zhao, "Thermal annealing of exfoliated graphene," *J. Nanomater.* **2013**, 1.
- ¹⁷B. C. Gundry, D. G. Cahill, and R. S. Averback, "Thermal conductance of metal-metal interfaces," *Phys. Rev. B* **72**, 245426 (2005).
- ¹⁸D. R. Lide, *CRC Handbook of Chemistry and Physics*, edited by D. R. Lide (Taylor & Francis, Boca Raton, FL, 2007).
- ¹⁹N. W. Ashcroft and D. N. Mermin, *Solid State Physics* (Harcourt College, New York, 1976).
- ²⁰H. C. Chien, D. J. Yao, M. J. Huang, and T. Y. Chang, "Thermal conductivity measurement and interface thermal resistance estimation using SiO₂ thin film," *Rev. Sci. Instrum.* **79**, 054902 (2008).
- ²¹A. Gupta, G. Chen, P. Joshi, S. Tadigadapa, and P. C. Eklund, "Raman scattering from high-frequency phonons in supported n-graphene layer films," *Nano Lett.* **6**, 2667 (2006).
- ²²S. Ghosh, W. Bao, D. L. Nika, S. Subrina, E. P. Pokatilov, C. N. Lau, and A. A. Balandin, "Dimensional crossover of thermal transport in few-layer graphene," *Nature Mater.* **9**, 555 (2010).
- ²³P. E. Hopkins, J. C. Duda, C. W. Petz, and J. A. Floro, "Controlling thermal conductance through quantum dot roughening at interfaces," *Phys. Rev. B* **84**, 035438 (2011).
- ²⁴W. G. Cullen, M. Yamamoto, K. M. Burson, J. H. Chen, C. Jang, L. Li, M. S. Fuhrer, and E. D. Williams, "High-fidelity conformation of graphene to SiO₂ topographic features," *Phys. Rev. Lett.* **105**, 215504 (2010).
- ²⁵S. P. Koenig, N. G. Boddeti, M. L. Dunn, and J. S. Bunch, "Ultrastrong adhesion of graphene membranes," *Nat. Nanotechnol.* **6**, 543 (2011).
- ²⁶Z. Chen, W. Jang, W. Bao, C. N. Lau, and C. Dames, "Thermal contact resistance between graphene and silicon dioxide," *Appl. Phys. Lett.* **95**, 161910 (2009).
- ²⁷K. F. Mak, C. H. Lui, and T. F. Heinz, "Measurement of the thermal conductance of the graphene/SiO₂ interface," *Appl. Phys. Lett.* **97**, 221904 (2010).
- ²⁸R. Prasher, "Acoustic mismatch model for thermal contact resistance of van der Waals contacts," *Appl. Phys. Lett.* **94**, 041905 (2009).
- ²⁹D. Nika, E. Pokatilov, A. Askerov, and A. A. Balandin, "Phonon thermal conduction in graphene: Role of Umklapp and edge roughness scattering," *Phys. Rev. B* **79**, 155413 (2009).
- ³⁰T. Tohei, A. Kuwabara, F. Oba, and I. Tanaka, "Debye temperature and stiffness of carbon and boron nitride polymorphs from first principles calculations," *Phys. Rev. B* **73**, 064304 (2006).
- ³¹C. Dames and G. Chen, "Theoretical phonon thermal conductivity of Si/Ge superlattice nanowires," *J. Appl. Phys.* **95**, 682 (2004).